CEAS-GNC-2024-006

EuroGNC Navigation Guidance Control CEAS Bristol, UK June 11th-13th 2024
University of BRISTOL ROYAL AERONAUTICAL SOCIETY AIAA

# Analytical characterization of the off-pointing probability for a spin-stabilized S/C subject to random particle impacts

**Andrea Pizzetti** GNC/AOCS Engineer, Deimos Space S.L.U., Flight Segment, 28760, Tres Cantos, Madrid, Spain. andrea.pizzetti@deimos-space.com

**Andrea Fabrizi** GNC/AOCS Engineer, Deimos Space S.L.U., Flight Segment, 28760, Tres Cantos, Madrid, Spain. andrea.fabrizi@deimos-space.com

*ABSTRACT*

**The pointing error is used as an important figure of merit since the first phases of the GNC design. However, its evaluation is not straightforward when it depends on parameters characterized by a high degree of uncertainty or when the system dynamics are driven by discrete random processes. A method is proposed to characterise analytically the off-pointing probability of a spin stabilised S/C subject to random particle impacts, based on the composition of the statistical distributions associated with the mission parameters. The Probe B2 of the Comet Interceptor mission is used as a case study. The mission goal is to complete a flyby around an as-yet-undiscovered comet. The probe is passively spin-stabilized and its ACS design and verification involves the development of a comet dust flow model to assess the off-pointing of the spin-axis due to multiple impacts of dust particles. The random variables considered are the number of impacts, the closest-approach distance, the mass of the impacting particle, as well as the impact position and velocity. Each of them is modeled with an appropriate distribution, accounting for the mission constraints and the properties of the probe B2 itself. Then, the probabilities of interest are derived and successfully cross-validated against the ones obtained from a Monte Carlo simulation campaign. Design decisions can be carried out quickly iterating between performance evaluation, parameters tuning and requirements definition, proving the effectiveness of the proposed method as an agile tool for preliminary pointing error evaluation in scenarios with discrete random processes, such as those involving particle impacts.**

**Keywords:** Stochastic · Pointing Budget · Spin · Impacts · Probability · Monte Carlo

## Nomenclature

| | | | | | |
|---|---|---|---|---|---|
| $N_{num}$ | = | numeric density | $\mu$ | = | mean |
| $N_{col}$ | = | column density | $\sigma$ | = | standard deviation |
| $d$ | = | distance from comet | $f_X(x)$ | = | probability density function |
| $s$ | = | distance from closest approach | $F_X(x)$ | = | cumulative density function |
| $\alpha$ | = | in-plane angle | $\bar{F}_X(x)$ | = | complementary cumulative density function |

| | | | | | |
|---|---|---|---|---|---|
| $\beta$ | = | out-of-plane angle | $\chi, \tau$ | = | scaling coefficients |
| $r_\odot$ | = | heliocentric distance | $h$ | = | momentum |
| $m$ | = | mass | $\theta$ | = | off-pointing angle |
| $v$ | = | velocity | $u$ | = | upper boundary |
| $ca$ | = | closest approach | $l$ | = | lower boundary |
| $r$ | = | radius | $T$ | = | torque |
| $\lambda$ | = | mean rate of occurence | $\omega$ | = | angular velocity |
| $n$ | = | particles number | $I$ | = | inertia |
| $a, b$ | = | fitting coefficients | $A$ | = | area |

# 1 Introduction

A common need in the first phases of any project is the preliminary performance evaluation and assessment of engineering budgets through relatively simple and quick analysis, to iterate with the customer on the requirements and select a baseline for the mission. Concerning the Guidance Navigation and Control (GNC) field, a pointing budget is generally performed to assess the impact of the different Pointing Error Source (PES) on the pointing performances of a Spacecraft (S/C). When uncertainties come into play, a Monte Carlo (MC) campaign is performed where deterministic models are simulated scattering at each MC shot the error source parameters according to the defined distributions. This allows characterizing the system performance metrics in terms of probabilities and associated confidence intervals. This activity is performed in any case during the Verification & Validation (V&V) phase to confirm the preliminary pointing budget assumptions.

The MC campaigns can become computationally expensive and time-consuming when rare events occur, such as impacts from debris or dust particles. In fact, in these cases the metrics of interest are largely influenced by the unlikely occurrences of such events and require a high number of MC shots to characterize the probability of satisfying the corresponding requirement with sufficient confidence. To address this issue, new tools emerged in recent years to perform preliminary pointing budgeting while preserving time and computational resources. In this context, the Pointing Error Engineering Toolbox (PEET) and the associated handbook from European Space Agency (ESA), set the standard for the industry practices [1]. The pointing error budget is carried out by combining additively each PES in a simplified way, if the central limit theorem applies, or by convolution of the Probability Density Functions (PDFS) otherwise [2]. Using the latter method, accurate results can be obtained, which can be then successfully cross-validated against MC simulations [3]. However, these methods can be applied only when the PES enter the model linearly.

A possible alternative is provided by $\mu$-analysis techniques [4], which allow studying linear systems affected by parametric and dynamic uncertainties with the goal of assessing the robust stability and the robust performance margins of the system. However, these methods cannot characterise the probability of occurrence of the identified worst cases. To bridge this gap, probabilistic $\mu$-analysis has been recently investigated. In this case, the aim is to find the probabilities related to the stability of the system and to the worst-case performance, given the uncertainties distribution [5]. Within the GNC domain, classical $\mu$-analysis has been applied for the preliminary pointing budget assessment within the BIOMASS mission [6] and for the verification of the pointing performance of Euclid [7], while probabilistic $\mu$-analysis has been used for assessment of pointing performance regions with probability bounds in presence of inertia matrix uncertainties [8]. Both the classical and probabilistic schemes exploit the Linear Fractional Transformation (LFT) model of an uncertain Linear Time Invariant (LTI) system: the parametric uncertainties are treated as independent Random Variables (RVS) and separated from the nominal closed-

loop system with a block diagonal operator. For this reason, they cannot be easily adapted to discrete stochastic processes such as those in systems subject to momentum transfer due to random impacts.

The problem addressed in this paper is the characterisation of the pointing error probability of a spin-stabilised s/c traveling through the dust coma of a comet, considering as a study case the Probe B2 of the Comet Interceptor mission by ESA. Generally, the approach followed for assessing the pointing performance of a s/c subject to random particle impacts is to integrate the discrete stochastic nature of the problem in the simulation framework, as done in [9], where hyper-velocity impacts of debris are incorporated as discrete random processes in the dynamics equations. The resulting stochastic differential equations allow to generate distributions for the evolution of the rotational kinetic energy of the body. For the problem at hand, an extensive MC analysis is performed in [10] to characterize the effect of dust particle impacts and to evaluate the likelihood of satisfying pointing and angular velocity requirements.

In this sense, our work can be framed as a step forward with respect to [10] and proposes a fully analytical method to characterise the probability associated with the system performance (e.g. pointing error) based on the composition of the probability distributions of the PEs in non-additive manners. The results are then compared against the probabilities computed from the MC simulation campaign. A similar approach has been explored in [11] for the characterization of multiple particle rebounds from rough wall surfaces, where the proposed PDFs are shown to fit experimental results. Differently, the problem addressed in this paper is of interest for the Attitude Control System (ACS) design of a s/c subject to particle impacts and, up to the authors' knowledge, it has never been characterized with a fully analytical model. The main advantage of our approach is that it can be efficiently used to avoid time-consuming MC simulations and to carry out design trade-offs in an agile way, allowing a quick iterative process between requirements definition, parameters tuning and performance evaluation.

The article is structured as follows. In *section 2*, the problem will be formally defined presenting the case study and framing each underlying parameter to its distribution. Then, in *section 3*, the probabilities related to the selected figure of merit will be obtained and compared to the MC simulation results. Moreover, examples of how this analytical approach can be used to relax requirements or tune parameters, avoiding lengthy design iterations, will be highlighted. Finally, in *section 4*, concluding remarks and considerations will be delivered.

# 2 Statistical Characterization

## 2.1 Problem Statement

The goal of the Comet Interceptor mission is to travel to an as-yet to discover comet, release two small probes (B1 and B2) from the SC-A and complete a flyby. The probe B2, provided by ESA, consists of a passive spin-stabilized platform and will be considered as a case study. The spin is achieved by means of a single Reaction Wheel (RW) for a total momentum vector of 4 Nms initially aligned with the velocity direction. A dust shield is located facing this direction to cover the probe from the impact of the dust particles. The shield has an octagonal shape with an area $A_{oct} = 0.41\,\mathrm{m}^2$ and a long diagonal $r_{out} = 0.38\,\mathrm{m}$. As it can be seen in *Figure 1*, the impact of a dust particle with mass $m$ and distance $r$ from the shield center off-sets the angular momentum vector from its nominal direction aligned with the encounter velocity vector. Consequently, the spin axis begins a precession-nutation dynamics around the angular momentum.

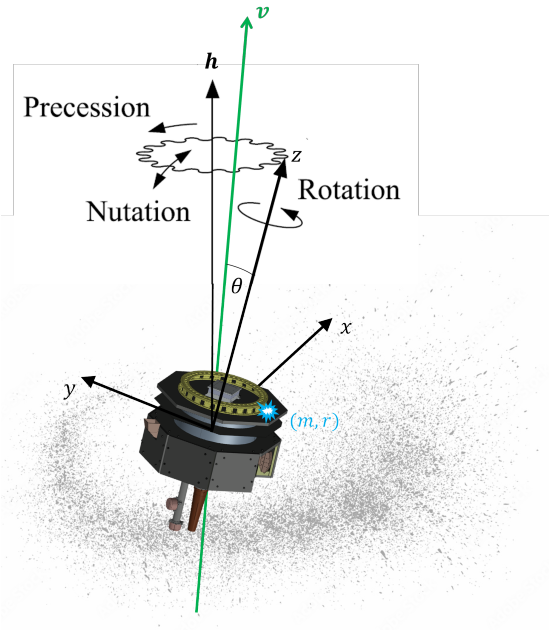


**Fig. 1 Problem statement**

The ACS design and verification involves the development of a comet dust flow model to assess the shift of the angular momentum vector of the s/c and the resulting off-pointing angle $\theta$ of the spin-axis due to multiple impacts of dust particles. In this context, the following main requirement is considered:

*The probe shall maintain a pointing error lower than 20° with respect to the velocity direction during the entire fly-by in 95% of the cases.*

The mission parameters are affected by a large degree of uncertainty due to the high variability of the comet population considered, as well as on the conditions of the fly-by and closest approach. For this reason, the determination of such probability is not straightforward with classical MC simulations, but it can be easily accomplished with the method proposed in the following sections.

## 2.2 Stochastic Modelling

The stochastic parameters considered in this problem are summarized in *Table 1*. Each of them will be now framed to the distribution that most gives an accurate representation of its variability. All the statistical concepts, distributions and formulas that will be used in the following paragraphs are detailed in *Appendix A*. When possible, the analytical PDFs will be validated against the histogram obtained from the MC simulation, where some assumptions are lifted off and more accurate models are employed. The MC simulation framework can be found in *Appendix B* for the interested reader.

| Name | RV | Distribution |
|---|---|---|
| Impact Mass | $M$ | $\sim \mathcal{L}\,(b+1, l_M, u_M)$ |
| Impact Velocity | $V$ | $\sim \mathcal{N}_{Tr}\,(\mu_V, \sigma_V, l_V, u_V)$ |
| Closest Approach | $CA$ | $\sim \mathcal{N}_{Tr}\,(\mu_{CA}, \sigma_{CA}, l_{CA}, u_{CA})$ |
| Impact Radius | $R$ | $\sim \mathcal{U}_{Oct}\,(r_{in}, r_{out})$ |
| Expected Impacts | $\Lambda$ | $\sim \mathcal{N}_{Tr}^{-1}\,(\mu_\Lambda, \sigma_\Lambda, l_\Lambda, u_\Lambda)$ |
| Impacts Number | $N$ | $\sim \mathcal{P}\,(\Lambda)$ |

**Table 1 Stochastic parameters and modeled distributions of the corresponding RV**

The trajectory of a flyby with relative encounter velocity $v$ is depicted in *Figure 2*. A flyby plane can be identified which intersects the comet nucleus and is perpendicular to the velocity vector. In this frame, the Sun direction is defined by the out-of-plane $\beta$ angle and the in-plane $\alpha$ angle. The intersection point of the velocity with the fly-by plane is called Closest Approach (CA). The distance of the s/c from the CA will be labelled $s$. The distance of the s/c from the comet will be therefore given by $d = \sqrt{s^2 + ca^2}$, where $ca$ is the distance of CA from the comet nucleus.

Due to Sun activity, the comet nucleus ejects dust particles, which form the coma. The EDCM data[1] is used to model the coma environment in terms of numeric density field $N_{num}$ (#/m$^3$) [12]. The data set provides discrete values of the number of particles per unit volume as function of distance from the comet, for different bins of particle radius and percentiles. The original bins classification can be mapped to the limit masses, assuming the particles as perfect spheres with an average bulk density equal to 570 kg/m$^3$ [12]. In this way the classification in *Table 2* is obtained.

The EDCM data points refer to the nominal trajectories of the SC-A and of the two probes B1 and B2. The data for the column density $N_{col}$ (#/m$^2$) is also present, which represents the integration of $N_{num}$ along the trajectory. The numeric density data of B2 ($ca$ = 200 km) at different distances from the comet

[1]Engineering Dust Coma Model (EDCM)

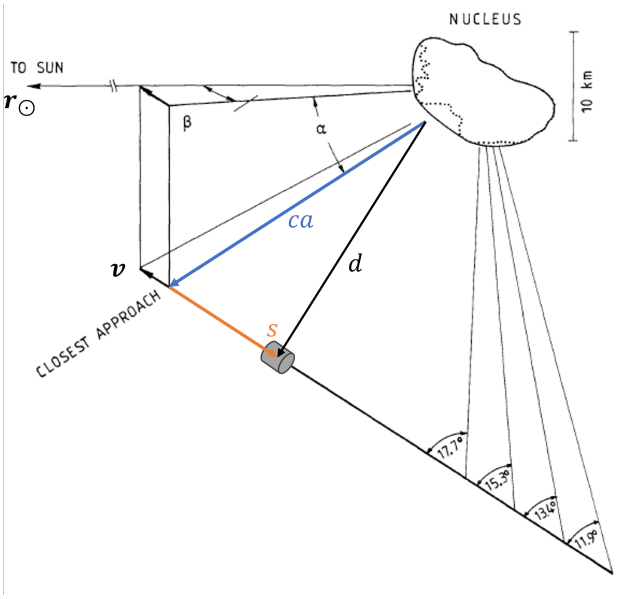


**Fig. 2 Flyby geometry. Re-adapted from [13]**

| $\mathcal{B}$ | $l_M$ [kg] | $u_M$ [kg] |
|---|---|---|
| 1 | 2.388E-15 | 7.534E-14 |
| 2 | 7.534E-14 | 2.388E-12 |
| 3 | 2.388E-12 | 7.534E-11 |
| 4 | 7.534E-11 | 2.388E-09 |
| 5 | 2.388E-09 | 7.534E-08 |
| 6 | 7.534E-08 | 2.388E-06 |
| 7 | 2.388E-06 | 7.534E-05 |
| 8 | 7.534E-05 | 2.388E-03 |
| 9 | 2.388E-03 | 7.534E-02 |
| 10 | 7.534E-02 | 2.388E+00 |
| 11 | 2.388E+00 | 7.534E+01 |

**Table 2 Bins classification**

is depicted in *Figure 3a*, together with the uncertainty ranges resulting from the percentiles. In *Figure 3b* same data is reported but as function of the particle mass/bin.

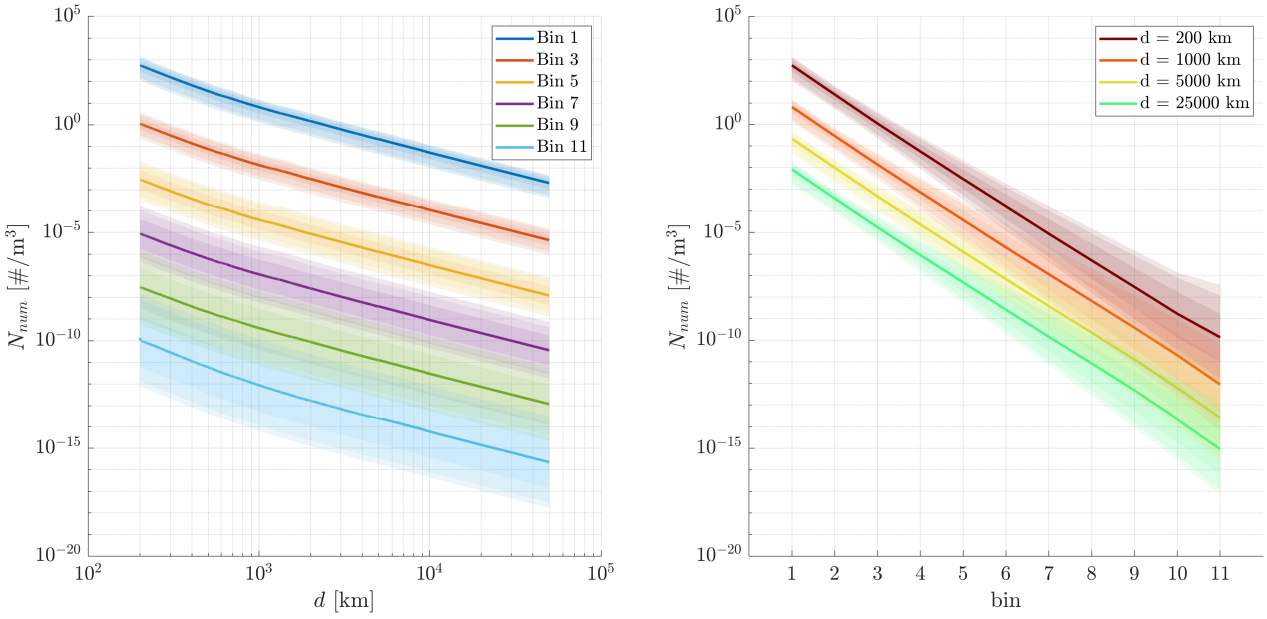


**(a) As function of distance from the comet**

**(b) As function of bin**

**Fig. 3 Numeric density data of B2 from EDCM**

A distinction can be made between high-density small particles and low-density large particles. The pointing errors generated by particles of mass lower than $\approx 10^{-8}$ kg and high numeric density can be assimilated to attitude jitter, with order of magnitudes similar to the one of sensors and actuators inaccuracies: under 0.03 ° at 99th percentile in the worst case flyby scenario [10]. Considering individually these impacts in the MC campaign is not necessary, given the computational cost increase that would be required and the limited impact they have with respect to the pointing requirement, which can be estimated considering them as a uniform pressure. Therefore, the bins from 1 to 5 will be discarded, in agreement with the simulations performed in [10].

On the other hand, large particles with low-density impact the S/C sparsely and transfer an angular momentum proportional to the distance between the impact point on the S/C surface and the Center of Gravity (COG). Large particles impacts can produce both a precession and nutation of the spinning axis. These particles belong to the bins from 6 to 11 and will be the only ones considered in the following analysis.

### 2.2.1 Impact Mass

Looking again at *Figure 3b*, it is possible to notice that the median numeric density is approximately linear in logarithmic scale with respect to the mass bin. It can thus be represented by the power law in (1).

$$N_{num}(m_{\mathcal{B}}, d) = a(d)\, m_{\mathcal{B}}^{-b(d)} \tag{1}$$

Where $m_{\mathcal{B}}$ is the reference mass of the bin $\mathcal{B}$, and $a(d)$ and $b(d)$ are unknown coefficients that can be determined by least-squares fitting, at each frozen distance.

The probability that an impact mass belongs to a given bin, fixed the distance to the comet, is obtained by dividing the numeric density at that bin by the global density across all the bins, as shown in (2).

$$P(m \in \mathcal{B}) = \frac{N_{num}(m_{\mathcal{B}}, d)}{\sum_{i=6}^{11} N_{num}(m_{\mathcal{B}_i}, d)} \tag{2}$$

By introducing $M$ as the continuous RV that describes the mass $m$ of a particle impact, its PDF is derived through differentiation of (2) with respect to the mass when $m_{\mathcal{B}} \to m$. The PDF is reported in (3) where $l_M$ and $u_M$ are respectively the lower and upper mass boundaries for the range of bins considered.

$$f_M(m) = \frac{\frac{d}{dm}\left(N_{num}(m, d)\right)}{\int_{l_M}^{u_M} \frac{d}{dm}\left(N_{num}(m, d)\right)\, dm} = \frac{\frac{d}{dm}\left(N_{num}(m, d)\right)}{N_{num}(u_M, d) - N_{num}(l_M, d)} \tag{3}$$

One can now observe from *Figure 3b* that the relative ratio of the median $N_{num}$ for different masses, which is the slope $b$ of the line in logarithmic scale, is approximately constant regardless of the distance. This implies the same relative likelihood of different masses impacting the S/C across the domain of $d$. This consideration allows to drop the dependency of $b$ on $d$, and consequently of the PDF as well, as shown in (4).

$$f_M(m) = \frac{\frac{d}{dm}\left(a(d)m^{-b}\right)}{a(d)u_M^{-b} - a(d)l_M^{-b}} = \frac{-bm^{-b-1}}{\left(u_M^{-b} - l_M^{-b}\right)} \tag{4}$$

Note that this expression is the same as the power-law PDF in *Appendix A* (33), when $b = \alpha - 1$. The distribution is evaluated across the mass range and, as depicted in *Figure 6a*, agrees with the MC results, other than the cases with large masses, whose low probability makes them difficult to be captured by the MC sampling.

### 2.2.2 Impact Velocity

Particles of 1.4 mg ejected from comet 1P/Halley were estimated to be in the velocity range of 22 to 45 m/s [14]. However, to model the impact velocity of the dust particles as seen by the probe, it is convenient to also study the distribution of the expected encounter velocity. The encounter velocity does not change the characteristics of the dust environment per se but it influences directly the off-pointing since the same impact mass will have a stronger momentum effect due to its larger relative speed. Intercept transfer trajectories to a population of 1700 comets were analyzed in a ESA study in 2019 [15]. As outcome, the expected variability of several fly-by geometry parameters was made available, and is reported in *Table 3a*. In particular, the distribution of expected encounter velocities is depicted in *Figure 4*.

Since the range of encounter velocity is several orders of magnitude larger than the absolute particle speed, this last is negligible and the impact velocity will be considered equal to the encounter velocity. To fit the distribution shown in *Figure 4*, $V$ is modelled as a Normal Truncated RV with the statistical parameters reported in *Table 3b*. Its PDF is compared to the MC samples in *Figure 6b*, showing excellent match. Note that the explicit formulation of $f_{\mathcal{N}_{Tr}}$ can be found in *Appendix A* (31).

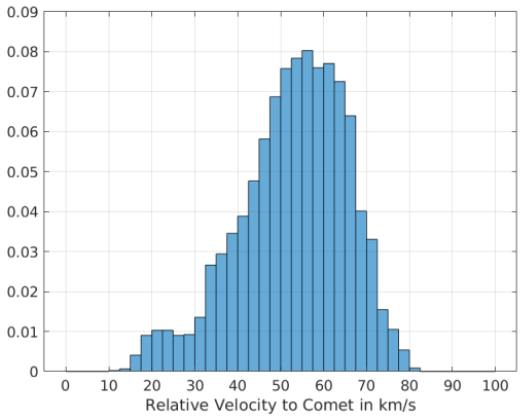


**Fig. 4 Expected encounter velocity distribution**

$$f_V(v) = f_{\mathcal{N}_{Tr}}(v, \mu_V, \sigma_V, l_V, u_V) \tag{5}$$

### 2.2.3 Closest Approach

A Normal Truncated RV is used to describe the distribution of $ca$ as well, with statistical parameters derived from the expected variability, as reported in *Table 3b*. Note that 5 km has been considered as a lower limit since it is the minimum comet nucleus radius considered in the EDCM.

$$f_{CA}(ca) = f_{\mathcal{N}_{Tr}}(ca, \mu_{CA}, \sigma_{CA}, l_{CA}, u_{CA}) \tag{6}$$

The numeric density depends on the distance from the comet and indirectly on the closest approach distance. Recalling that $d = \sqrt{s^2 + ca^2}$, an increase in $ca$ will result in a lower numeric density for the same $s$. For small variations of $ca$ with respect to the reference value $\widehat{ca}$, the scaling laws proposed in [16] can be used to scale the numeric density (7) and the column density (8) respectively.

$$N_{num}(d)\Big|_{ca} = \underbrace{\left(\frac{\widehat{ca}^2}{ca^2}\right)}_{\chi} \widehat{N}_{num}(d)\Big|_{\widehat{ca}} \tag{7}$$

$$N_{col} = \left(\frac{\widehat{ca}}{ca}\right) \widehat{N}_{col} \tag{8}$$

However, (7) is accurate only for the numeric density evaluated at CA (i.e. $s = 0$). This can be seen in *Figure 5*, where the numeric density data is plotted for the three S/C trajectories in log-log scale and (7) is used to scale the B2 data at the CA of B1 (500 km) and of SC-A (1000 km). Ideally, the scaled B2 data (dashed lines) should match the B1 and SC-A data, but large errors are observed.

$N_{num}$ should converge at very large distances from the comet, regardless of $ca$. To account for this, the scaling coefficient in (7) is modified to depend on $d$ instead of $ca$. In this way the scaling law in (9) is obtained. Note that $\chi_{new}$ matches the previous scaling when $s = 0$ and goes to 1 for $s \to \infty$. $N_{num}$ can be written as function of $s$ and $ca$ to be easily evaluated at each MC shot (fixed $ca$) and along time (varying $s$). The data scaled with the new coefficient (dotted lines) is now in better agreement.

$$N_{num}(s, ca) = \underbrace{\left(\frac{\widehat{d}^2}{d^2}\right)}_{\chi_{new}} \widehat{N}_{num}(s, ca) = \frac{s^2 + \widehat{ca}^2}{s^2 + ca^2} \widehat{N}_{num}(s, ca) \tag{9}$$

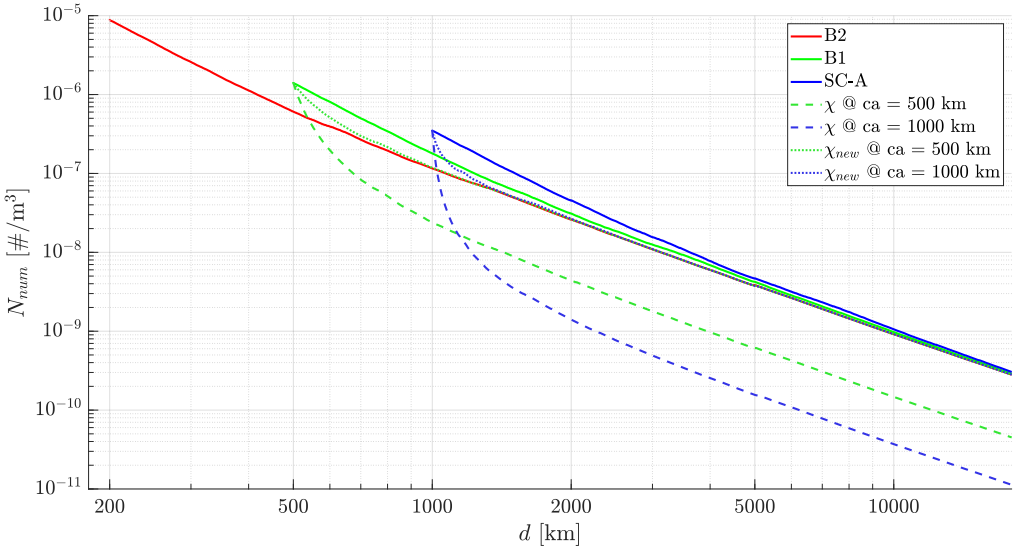


**Fig. 5 Median numeric density (bin 7) along the trajectories of the three s/c and scaling of B2 data to the closest approach distances of B1 and SC-A using (7) (dashed lines) and using (9) (dotted lines)**

### *2.2.4 Flyby Geometry*

The numeric density field is influenced by other parameters related to the geometry of the encounter. Mainly, these are the $\alpha$ and $\beta$ angles, which skew the density distribution, and the heliocentric distance $r_\odot$, which affects the dust production rate.

Since the dust emission intensity at the comet surface is maximum in the Sun direction, changes in $\alpha$ and $\beta$ reduce the numeric density expected at CA and skew the point of maximum depending on the solar zenith angle. Scaling laws for numeric density are not straightforward to derive analytically. For what concerns column density, a scaling is proposed in [16]. Within the expected variability for these parameters, the scaling factor is always close and below the nominal value of 1, obtained for $\alpha$ and $\beta$ equal to zero. They will be thus considered constant and equal to zero to be conservative.

Concerning the heliocentric distance, the results remain valid for solar flux variations up to the factor of 2 [12], which is well inside the variability of the comet population analyzed for the mission [15]. Therefore, also this parameter will be set to the default value of 1 AU.

| | |
|---|---|
| $v$ [km/s] | 10/70 |
| $ca$ [km] | $400 \pm 200(1\sigma)$ |
| $\alpha$ [deg] | 0 |
| $\beta$ [deg] | −45/45 |
| $r_\odot$ [AU] | 0.9/1.2 |

**(a) Expected variability range**

| | $\mu$ | $\sigma$ | $l$ | $u$ |
|---|---|---|---|---|
| $v$ [km/s] | 50 | 15 | 10 | 70 |
| $ca$ [km] | 400 | 200 | 5 | 1200 |
| $\alpha, \beta$ [deg] | = 0 | | | |
| $r_\odot$ [AU] | = 1 | | | |

**(b) Statistical parameters used**

**Table 3 Uncertain fly-by environment parameters**

### 2.2.5 Impact Radius

The impact radius $r$ is modelled as a RV whose distribution assigns uniformly the lever arm value on the dust shield surface. This distribution is analytically derived in *subsubsection A.2.7*, considering a polygonal area of any sides. The probability is maximum in correspondence of the circumference of the inscribed circle, and minimum at zero and at the circumscribed circle. For an octagon with circumradius $r_{out}$ and inradius $r_{in}$, the PDF is reported in (10) and plotted in *Figure 6d* against the norm of the position vector of each impact in the MC simulation, showing excellent agreement.

$$f_R(r) = \begin{cases} \frac{2\pi r}{A_{oct}} & r \leq r_{in} \\ \frac{2\pi r}{A_{oct}} \left(1 - \frac{8}{\pi} \operatorname{acos}\left(\frac{r_{in}}{r}\right)\right) & r_{in} < r \leq r_{out} \\ 0 & r > r_{out} \end{cases} \tag{10}$$

### 2.2.6 Expected Impacts

The expected impacts $\lambda$ are defined as the mean number of particles encountered during any flyby. Considering the reference flyby case with $\widehat{ca} = 200\,\text{km}$, the corresponding expected impacts $\widehat{\lambda}$ can be computed from the $50th$ percentile of the column density data, summing the values across all the bins considered and multiplying for the impact surface, as shown in (11). Note that this assumes the area to be always aligned with the velocity direction.

$$\widehat{\lambda} = A_{oct} \sum_{i=6}^{11} \widehat{N}_{col}^{\mathcal{B}_i} \tag{11}$$

To incorporate the influence of the $ca$ variability, a generalized expression is obtained in (12), recalling the scaling law in (8).

$$\lambda(ca) = A_{oct} \sum_{i=6}^{11} N_{col}^{\mathcal{B}_i} = A_{oct} \sum_{i=6}^{11} \frac{\widehat{ca}}{ca} \widehat{N}_{col}^{\mathcal{B}_i} = \widehat{\lambda}\, \widehat{ca}\, \frac{1}{ca} \tag{12}$$

When deriving $\Lambda$, the RV that describes $\lambda$, one should take care that this last is dependant on a second RV, $CA$, which follows a Normal Truncated distribution. Given that $\lambda$ is equal to a constant multiplied by the inverse of $ca$, the distribution of $\Lambda$ will follow a Normal Truncated Inverse with statistics parameters re-scaled by that constant. The PDF is written explicitly in (13) and the resulting distribution is shown in *Figure 6e*.

$$\begin{gathered} f_\Lambda(\lambda) = f_{\mathcal{N}_{Tr}^{-1}}(\lambda, \mu_\Lambda, \sigma_\Lambda, l_\Lambda, u_\Lambda) \\ \mu_\Lambda = \frac{\mu_{CA}}{\widehat{\lambda}\,\widehat{ca}} \quad \sigma_\Lambda = \frac{\sigma_{CA}}{\widehat{\lambda}\,\widehat{ca}} \quad l_\Lambda = \frac{l_{CA}}{\widehat{\lambda}\,\widehat{ca}} \quad u_\Lambda = \frac{u_{CA}}{\widehat{\lambda}\,\widehat{ca}} \end{gathered} \tag{13}$$

### 2.2.7 Impacts Number

Given a fixed mean rate of occurrence $\lambda$, a Poisson distribution can be considered for modelling the number of consequent impacts $N$ during the flyby. Since $\Lambda$ has its own distribution, however, the distribution of $N$ follows a Conditional PDF subjected to $\Lambda = \lambda$.

$$f_{N|\lambda}(n) = \frac{\lambda^n e^{-\lambda}}{n!} \tag{14}$$

To obtain the impacts number distribution that accounts for the entire variability of $\Lambda$, one has to compute the Marginal PDF of $N$, by integrating the Joint PDF over the domain of $\Lambda$, as shown in *Appendix A*.

$$f_N(n) = \int_0^\infty f_{N\Lambda}(n,\lambda)d\lambda = \int_0^\infty f_{N|\lambda}(n) f_\Lambda(\lambda) d\lambda \tag{15}$$

Where the relation in *Appendix A* (27) has been exploited. In *Figure 6f* the integral is compared against the distribution of the sum of the impacts along the entire flyby for every MC shot. A good match is observed. The MC results appear to be slightly skewed towards lower number of impacts, possibly because of the limit of number of impacts per time step imposed in the impact model algorithm, which increases the probability of having a total number of impacts that is lower than the one expected by the analytical result.

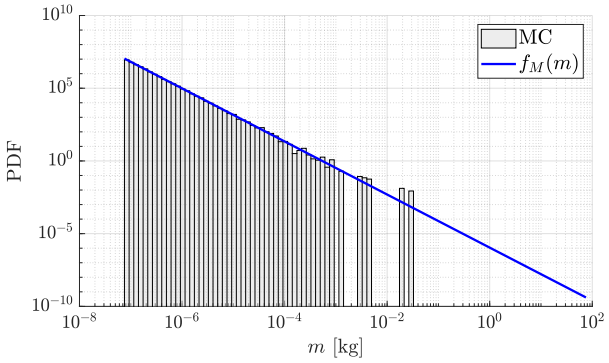


**(a) Impact Mass**

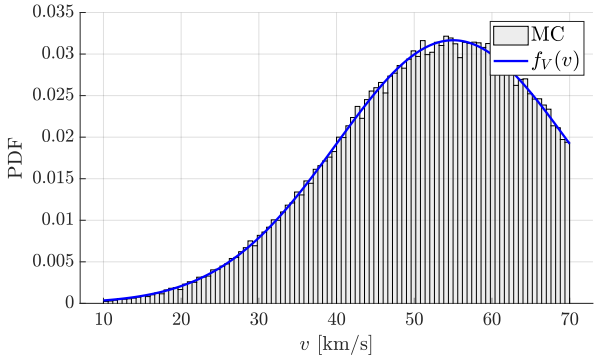


**(b) Impact Velocity**

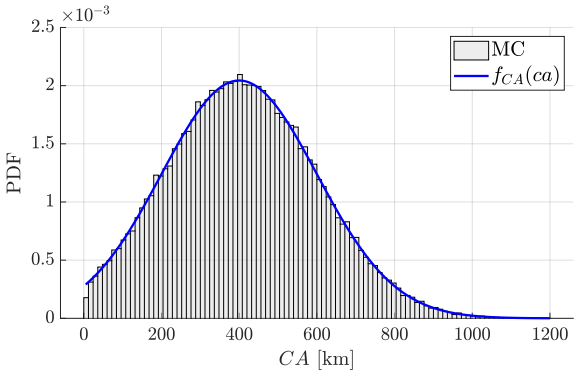


**(c) Closest Approach**

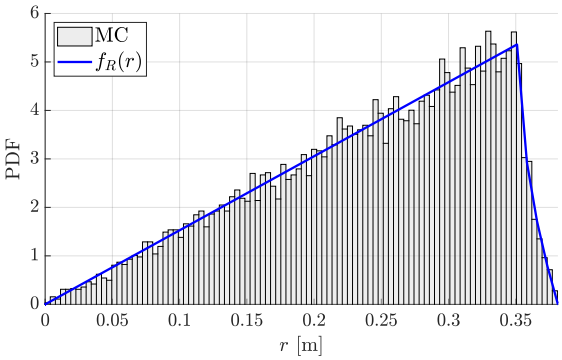


**(d) Impact Radius**

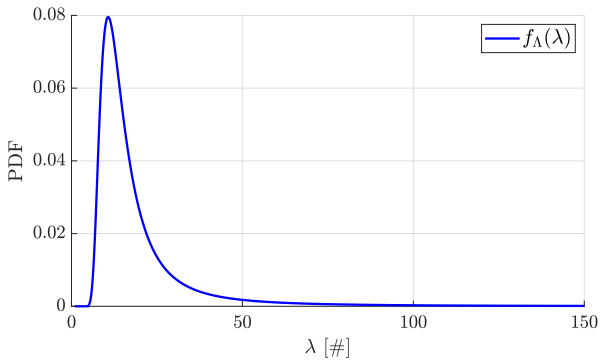


**(e) Expected Impacts**

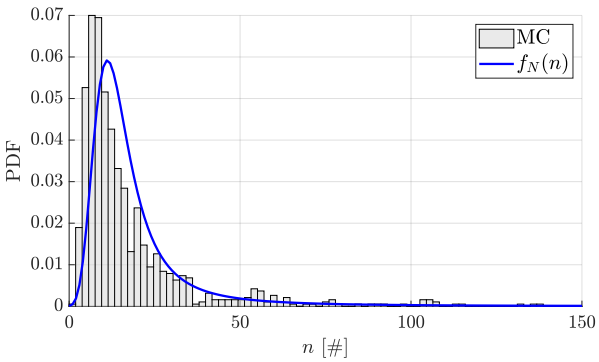


**(f) Impacts Number**

**Fig. 6 Analytical PDF of stochastic parameters against distribution of the MC results**

# 3 Off-Pointing Characterisation

## 3.1 MC Results

An extensive MC campaign of 1000 shots is performed using the framework presented in *Appendix B* to check the consistency of the modelled distributions and for cross-validation of the analytical probabilities, whose derivation will be outlined in the next section.

The numeric density data used in the MC is the median density (50th percentile) for the bins from 6 to 11. The initial position $s_0$ is set at 57000 km, which is outside the EDCM data domain, in order to cover the entire comet density field. The sampling time of the simulation is set to 0.025 s and the total simulation time is 7700 s. At the minimum relative velocity of 10 km/s, this time is enough to reach the CA and arrive at a final distance of 20 000 km, where the numeric density for each bin is more than 5 orders of magnitude lower than at CA, as it can be seen in *Figure 3b*.

The $95th$, $90th$, $75th$ and $50th$ percentile estimation of the pointing error of the spin-axis with respect to the velocity direction is reported in *Figure 7*, together with the 90% confidence bands over the full MC campaign results. The critical phase is just a few km before CA, where even a single high-mass low-probability impact particle can cause an abrupt change in the S/C momentum and a large off-pointing angle.

As it can be seen, the requirement is not currently respected in the 95% of the cases but rather on the 90%. Moreover, a non-linear behavior can be observed when moving towards larger percentiles, with an off-pointing probability increase occurring way before CA, which captures the occurrence of the rare events of low-density large particle impacts.

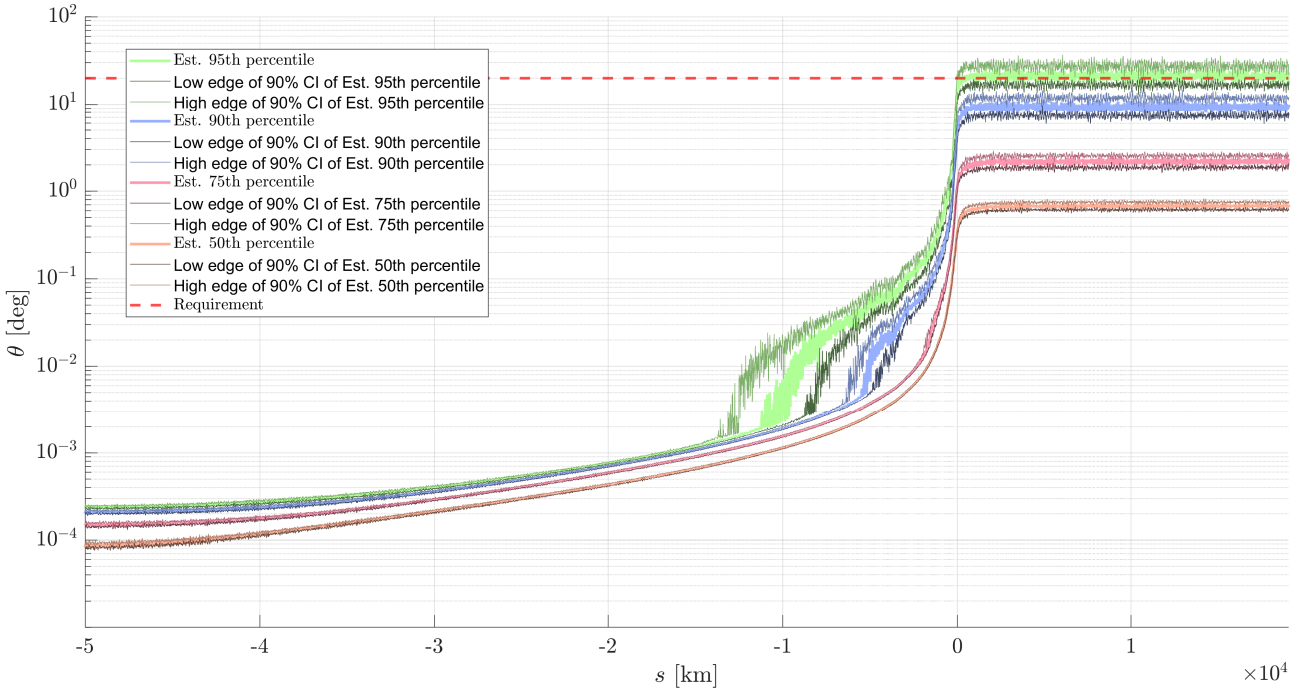


**Fig. 7 Percentiles of the pointing error with 90% confidence bands from MC simulation results**

## 3.2 Probability Derivation

This section aims to replicate analytically the results of the MC campaign by applying probability laws and combining the distributions of the stochastic parameters driving the process, previously summarized in *Table 1*. Before proceeding, some metrics are declared:

- **Off-Pointing** Defined as the worst-case angle $\theta$ of the body pointing axis with respect to the velocity direction. For spin-axis stabilized S/C, the worst case off-pointing due to nutation and precession can be quantified by (16), where $h$ is the momentum of the S/C along the spin axis and $h_\perp$ is the total change in transverse angular momentum [15].

$$\theta\,(m, v, r) = 2\left(\frac{h_\perp}{h}\right) = \frac{2\,m\,v\,r}{h} \tag{16}$$

- **Critical Radius** Defined as the impact radius $r_{cr}$ that cause an off-pointing larger than a requirement $\theta_{req}$, as per (17).

$$\theta\,(m, v, r_{cr}) > \theta_{req} \quad \rightarrow \quad r_{cr}\left(m, v, \theta_{req}\right) = \frac{1}{2}\frac{h\,\theta_{req}}{m\,v} \tag{17}$$

- **Critical Impact** Defined as the impact caused by a particle whose impact radius is larger than the critical, for a given mass and velocity.

The focus of the following paragraphs is to find the probability of having critical impacts at any given requirement $\theta_{req}$, i.e. find the probability of an off-pointing larger than $\theta_{req}$ considering the variability of all the stochastic parameters.

### *3.2.1 Single Critical Impact Probability*

The probability of a single critical impact at any $m$ and $v$ is simply given by the Complementary Cumulative Density Function (CCDF) of $R$ evaluated at all the corresponding $r_{cr}(m, v, \theta)$. The corresponding probability for a requirement of 20° is shown in *Figure 8* as a surface and contour plots.

$$P\left(M = m, V = v, R > r_{cr_{(m,v,\theta)}}\right) = \int_{r_{cr(m,v,\theta)}}^{+\infty} f_R(r)dr = \bar{F}_R(r_{cr_{(m,v,\theta)}}) \tag{18}$$

To evaluate the overall probability and account for the distributions of $M$ and $V$, the Joint PDF must be integrated as shown in (19): firstly, the lower and upper bounds of the integrals are replaced with the bounds of the distributions; secondly, since all the three RVs are independent, the joint PDF is expressed multiplying each PDF; finally, the innermost integral is substituted with (18).

$$\begin{aligned} P\left(R > r_{cr(\theta)}\right) &= \int_{-\infty}^{+\infty}\int_{-\infty}^{+\infty}\int_{r_{cr(m,v,\theta)}}^{+\infty} f_{VMR}\,(v, m, r)\,dr\,dm\,dv = \\ &= \int_{l_V}^{u_V} f_V(v)\int_{l_M}^{u_M} f_M(m)\int_{r_{cr(m,v,\theta)}}^{r_{out}} f_R(r)\,dr\,dm\,dv = \\ &= \int_{l_V}^{u_V} f_V(v)\int_{l_M}^{u_M} f_M(m)\bar{F}_R(r_{cr(m,v,\theta)})\,dm\,dv \end{aligned} \tag{19}$$

The procedure is iterated for every value of $\theta_{req}$, obtaining the plot in *Figure 9*. These analytical results are compared against the MC probabilities, obtained by checking at each impact if the impact radius is higher than the critical one at that impact mass and velocity. A good match is observed between analytical and MC results.

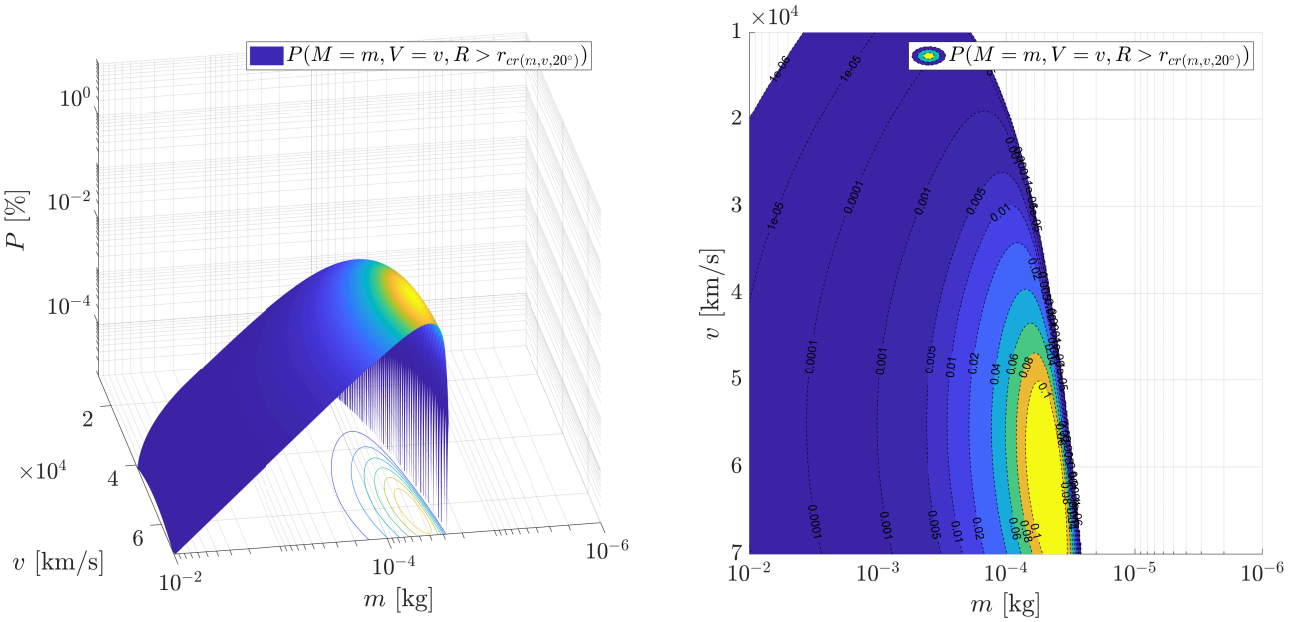


**(a) Surface** **(b) Contour**

**Fig. 8 Single impact probability of 20° off-pointing for any mass and velocity**

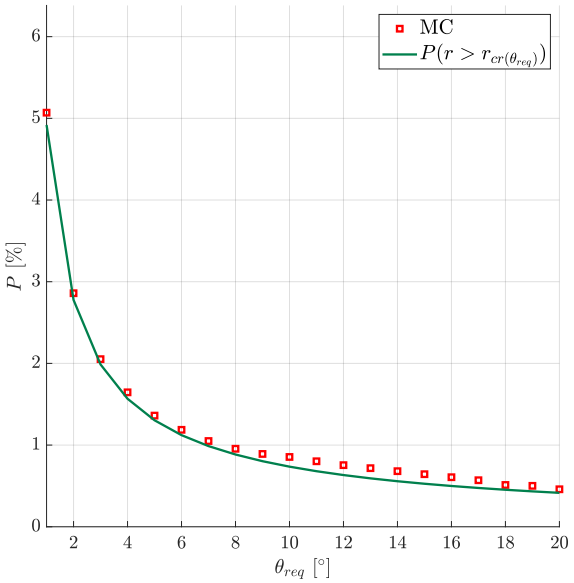


**Fig. 9 Single critical impact probability for different requirements**

### *3.2.2 Multiple Critical Impact Probability*

To assess the probability of violating the pointing requirement during the entire fly-by, the probability of having at least one critical impact out of $n$ impacts must be computed.

The probability of an event occurring at least once is 1 minus the probability of the event never occurring. Since $P(R_i > r_{cr_{(\theta)}})$ is the same regardless of $i = 1, \ldots, n$, the probability of at least one critical impact out of $n$ is given by (20).

$$
\begin{aligned}
P_{one}^{\boxed{n}}\left(R > r_{cr_{(\theta)}}\right) &= \left[P\left(R_1 > r_{cr_{(\theta)}}\right) \cup P\left(R_2 > r_{cr_{(\theta)}}\right) \cup \cdots \cup P\left(R_n > r_{cr_{(\theta)}}\right)\right] = \\
&= 1 - \left[P\left(R_1 \leq r_{cr_{(\theta)}}\right) \cap P\left(R_2 \leq r_{cr_{(\theta)}}\right) \cap \cdots \cap P\left(R_n \leq r_{cr_{(\theta)}}\right)\right] = \\
&= 1 - \left[P\left(R \leq r_{cr_{(\theta)}}\right)\right]^n = \\
&= 1 - \left[1 - P\left(R > r_{cr_{(\theta)}}\right)\right]^n
\end{aligned} \tag{20}
$$

The distribution of $N$ can be accounted for by computing the probability of having at the same time $N = n$ and $P_{one}^{\boxed{n}}$. Given these events are independent, (21) is obtained. Note that $P(N = n) = f_N(n)$ as the PDF is discrete.

$$
P_{one}\left(N = n, R > r_{cr_{(\theta)}}\right) = f_N(n)\, P_{one}^{\boxed{n}}\left(R > r_{cr_{(\theta)}}\right) \tag{21}
$$

The probability is evaluated across the domain of $n$. By using again a requirement of 20° as an example, the plot in *Figure 10a* is obtained.

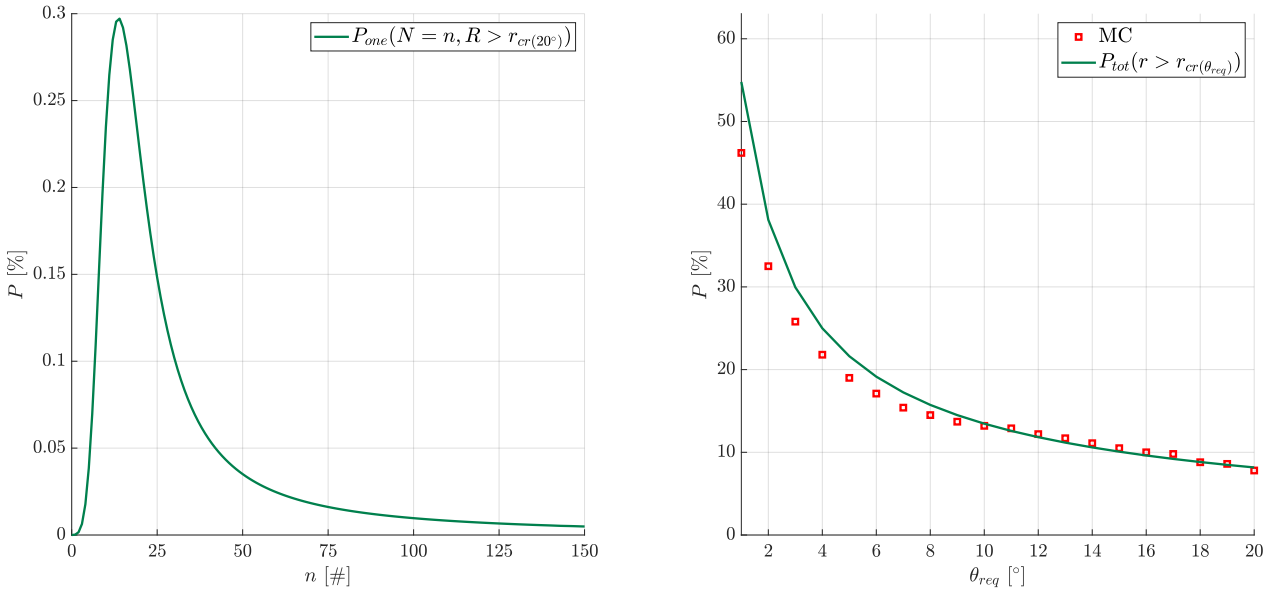


**(a) For any number of impacts ($\theta_{req} = 20°$)** **(b) For different requirements**

**Fig. 10 Multiple impact probability of at least one critical impact**

Finally, the overall probability of violating the pointing requirement in all the possible cases of $n$ is computed with (22), summing the probabilities at each $n = k$, since all the events are disjoint.

$$
P_{tot}\left(R > r_{cr_{(\theta)}}\right) = \sum_{k=1}^{\infty} P_{one}\left(N = k, R > r_{cr_{(\theta)}}\right) \tag{22}
$$

The probability is evaluated for different pointing requirements, obtaining the plot in *Figure 10b*. The MC probability is plotted as well, obtained by dividing the number of runs not respecting the requirement for the total number of runs.

It is observed that the MC probability gets more optimistic than the analytical one with lower requirement angles. This could be traceable to the skewness already noticed in *Figure 6f*, since between *Figure 9* and *Figure 10b* the only stochastic parameter introduced is the number of impacts $n$ and its distribution $f_N(n)$. In any case, differences in the results were expected, since the deterministic MC simulator and the analytical model differ in some relevant points:

- Consecutive impacts along the fly-by modify the s/c momentum and therefore the critical radius at the same conditions is time-varying: this phenomenon cannot be considered in the probabilistic study, which is basically time-frozen, while it is inherently present in the MC campaign.
- For the same reason, also the impact area is time-varying as along time the off-pointing reduces the actual impact area to its projection along the velocity direction.
- Due to inertia principal axis misalignment with respect to the spin axis, after the spin is achieved, an initial small nutation and low off-pointing is present since the beginning of the simulation, which was not accounted for in the analytical derivation.
- A limit of 10 impacts per time step was used during each MC shot for computational feasibility reasons. This has a direct effect on the skewness of the distribution of $N$, as previously explained.
- Finally, the 1000 shots used for the MC campaign may not be sufficient to provide significant statistical confidence in the results, considering the rarity of the events at play.

However, the overall good match observed allows to state that the analytical derivation of probability can be considered an effective tool for the preliminary analysis of the off-pointing angle in an agile way with respect to cumbersome and time-consuming MC simulations. To give an idea of the benchmark metrics, the analytical model delivers each off-pointing requirement probability point in about 0.9 s (18 s for the full 20 points of the plot in *Figure 10b*) against $\approx$ 4 hours required for a 1000-shots MC campaign, using MATLAB r2023b on a Dell Latitude 5440 (Intel i7-1370p).

## 3.3 Iterative Design

Given a pointing requirement, the analytical approach presented so far may be used either to tune design parameters for its fulfillment, or to relax the requirement itself on the go. In fact, the variability of these changes on the pointing budget can be assessed in a quick way by simply iterating the procedure presented so far instead of running a different MC campaign for each frozen parameter, therefore saving hours of time.

Consider the requirement introduced in *subsection 2.1*. As it can be seen in *Figure 10b*, the 95% probability is not currently fulfilled: in fact, the probability of having an off-pointing larger than 20° is closer to 10% than 5%.

### *3.3.1 Relaxing the Requirement*

One may think to relax the afore-mentioned requirement by introducing a limit of applicability only to not-destructing impacts. In fact, the highest bins are characterized by mass on the order of magnitude of kg, which would destroy the probe rather than off-point its spin direction. The off-pointing requirement in this sense would cover only impacts of not-destroying masses, which have only consequences on the off-pointing. This limitation can be easily introduced by lowering the upper boundary $u_M$, used for the derivation of the impact mass PDF in (4).

The new probability trends obtained using different upper limits for the impact mass are reported in *Figure 11a*. Lower mass limits basically translate into lower probabilities of off-pointing, especially at larger requirement angles. This can be explained by the fact that small degrees of off-pointing are inevitable, due to the small-to-medium masses that are never excluded; on the other hand, the large masses are the contributors to the relatively high probability of off-pointing at larger requirement angles. As it can be seen, setting a maximum mass limit to 0.1 g would allow to fulfill the desired probability.

### 3.3.2 *Tuning a Parameter*

On the other hand, an example of a design parameter that could be tuned is the s/c momentum, which dictates the gyroscopic stiffness of the probe. With a larger spin rate, the impact of particles is expected to cause lower off-pointings, according to (16). This is verified in *Figure 11b* for different s/c momentum values. The consequence in this case is an entire offset of the probability trend, as the gyroscopic stiffness reduces the off-pointing angle regardless of the mass of the particle. By increasing the s/c momentum to 8 Nms, the probability would go down to 5%.

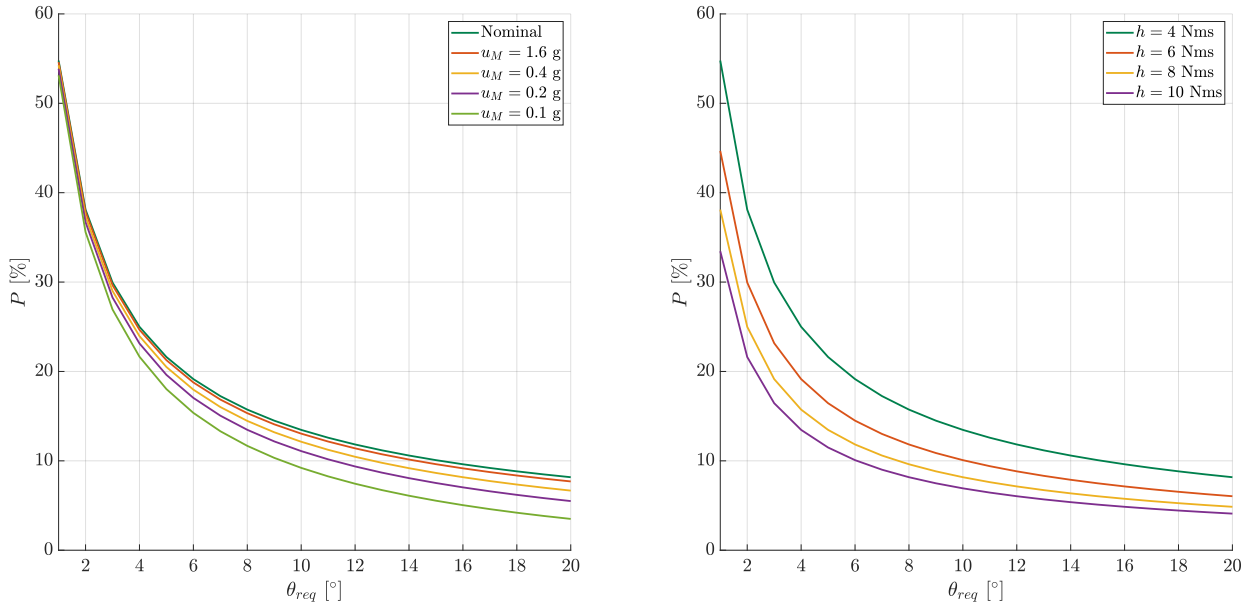


**(a) With different upper mass limits** **(b) With different s/c momentum**

**Fig. 11 Multiple critical impact probability for different off-pointing requirements, tuning parameters**

# 4 Conclusions

Some main contributions to the field of preliminary pointing budgeting can be identified, stemming from the work presented in the article:

- The identification of the stochastic parameters that best capture the variability of the scenario under study and their framing to precisely formulated distributions.
- The derivation of a fully analytical model to characterize the pointing error metrics of a spin-stabilized s/c in case of uncertainties and discrete random events.
- A validation of the results of such model against the ones of a deterministic MC campaign to prove the effectiveness of replacing the time-consuming simulations with the analytical model, at least at preliminary design stages.
- A clear framework and methodology of application of statistical concepts and operations, which the interested readers may extrapolate to other domains.

Although the analytical tool presented in this article seems promising, it should be noted that inherent limitations characterize it. Some stochastic parameters cannot be framed straightforwardly due to a poor understanding of the underlying phenomena. Moreover, impacts were assumed to be completely elastic. In reality, a momentum enhancement factor is typically introduced to describe the increase in momentum transfer due to hyper-velocity impact processes, such as cratering [17]. Future works may address these points.

For the mentioned reasons, a detailed MC simulation is expected to be performed in any case after the tuning of the design parameters (e.g. mass limit or S/C momentum), removing most of the assumptions and refining the deterministic models. In this sense, it is beneficial to stress that the method presented in this article is expected to be used only at a preliminary stage, as the degree of complexity that can be modeled analytically is inherently limited.

Future works may be foreseen on the application of the same method to different applications and domains. The main complexity that one encounters when trying to do so, is to identify how the RVS interact with each other and to fit each RV to the right PDF. The universe of possible distribution shapes is vast: the association of the correct distribution to the empiric data set, or to the expected variability of the RV, should be in principle feasible. If no match is found for a particular RV, assumptions have to be introduced. Once each RV is characterized and framed, it is of outermost importance the selection of a figure of merit to be linked with the RVS through an analytical relation, such as done in (16) with the off-pointing angle. After these metrics are identified, the probability derivation of the figure of merit can be accomplished, by carefully applying the rules of composition of PDFS.

In problems where the characterisation of the RVS is not the main driver of the dynamics or where normal distributions can be employed, simpler methods such as the ones mentioned in the introduction may be used. For those cases where the proposed method is applicable, however, accurate results can be delivered in a fraction of time with respect to a full MC campaign. The technique presented can thus be considered a valid addition to the tools available to engineers dealing with preliminary pointing budgeting.

# Appendix

# A Statistics

Some concepts and formulas concerning the statistics domain extensively used in the article are detailed in the following paragraphs.

## A.1 Probability

The probability $P$ of an outcome is obtained by counting the number of occurrences of that outcome along all the tries. Some general rules apply:

- If two events are independent, the probability of them occurring at the same time is the product of their probabilities.
- If two events are disjoint, i.e. mutually exclusive, the probability of either one of them occurring is the sum of their probabilities.
- The probability of an event not occurring is 1 minus the probability of the event.
- The probability of an event occurring at least once is 1 minus the probability of the event never occurring.

The PDF of a continuous RV $X$ is the function $f_X(x)$ such that the probability of $X$ falling between values $a$ and $b$ is given by (23).

$$P(a \leq x \leq b) = \int_a^b f_X(x)dx \tag{23}$$

The Cumulative Density Function (CDF) and CCDF are the functions $F_X(x)$ and $\bar{F}_X(x)$ that give the probability of $X$ being respectively smaller or larger than $x$. From the PDF one may obtain the CDF and the CCDF, by changing the integral boundaries, as shown in (24) and (25).

$$P(X \leq x) = F_X(x) = \int_{-\infty}^{x} f_X(x)dx \tag{24}$$

$$P(X > x) = \bar{F}_X(x) = \int_{x}^{\infty} f_X(x)dx \tag{25}$$

These formulas can be extended to the case with two RVS $X$ and $Y$. In this case, the Joint PDF is the two-variables function $f_{XY}(x, y)$ that gives the probability distribution on all the possible combinations of $x$ and $y$. The Joint PDF is used to obtain the Conditional PDF of $X$ given $Y = y$ and the Marginal PDF of $X$, given by (26) and (27) respectively. The former embeds the probability of $X$ given that $Y$ assumed a certain value $y$. The latter expresses the probability of $X$ accounting for all the variability of $Y$: it can be thought as averaging the conditional probability of the first RV over the distribution of all the values of the second RV.

$$f_{X|y}(x) = \frac{f_{XY}(x, y)}{f_Y(y)} \tag{26}$$

$$f_X(x) = \int_{-\infty}^{\infty} f_{XY}(x, y)dy \tag{27}$$

Note that the Joint PDF of two independent RVS is simply given by (28). In this case, the Marginal PDF is equivalent to the normal one as the value of one variable does not influence the other.

$$f_{XY}(x, y) = f_X(x)f_Y(y) \quad \text{if } X \perp\!\!\!\perp Y \tag{28}$$

## A.2 Distributions

### *A.2.1 Uniform*

A uniform distribution returns the same probability of an event in between the domain bounds. Its PDF is given by (29) and has a simple rectangular shape.

$$f_{\mathcal{U}}(x, l, u) = \begin{cases} 0 & x \leq l \\ \frac{2}{(u-l)} & l < x \leq u \\ 0 & x > u \end{cases} \tag{29}$$

### *A.2.2 Normal*

The PDF of a normal distribution is reported in (30), where $\mu$ and $\sigma$ are respectively the mean and the standard deviation of the RV.

$$f_{\mathcal{N}}(x, \mu, \sigma) = \frac{1}{\sigma\sqrt{2\pi}} e^{-\frac{1}{2}\left(\frac{x-\mu}{\sigma}\right)^2} \tag{30}$$

When the RV domain is constrained by upper and/or lower boundaries, this distribution can be extended to a Normal Truncated. Its PDF is given in (31), where $l$ and $u$ are respectively the lower and upper bounds of the RV.

$$f_{\mathcal{N}_{Tr}}(x, \mu, \sigma, l, u) = \frac{1}{\sigma} \frac{f_{\mathcal{N}}(x, \mu, \sigma)}{F_{\mathcal{N}}(u, \mu, \sigma) - F_{\mathcal{N}}(l, \mu, \sigma)} \tag{31}$$

Finally, to model the distribution of the inverse of a RV, the Normal Truncated Inverse distribution can be introduced, which is obtained using (32).

$$f_{\mathcal{N}_{Tr}^{-1}}(x, \mu, \sigma, l, u) = \frac{1}{x^2} f_{\mathcal{N}_{Tr}}\left(\frac{1}{x}, \mu, \sigma, l, u\right) \tag{32}$$

### *A.2.3 Power-Law*

As the name suggests, this distribution is related to a probability that changes with the power of the RV to a coefficient $\alpha$. Its PDF is written in (33), with the domain ranging from $l$ to $u$ [18].

$$f_{\mathcal{L}}(x, \alpha, l, u) = \frac{(1-\alpha)x^{-\alpha}}{u^{1-\alpha} - l^{1-\alpha}} \tag{33}$$

### *A.2.4 Poisson*

This distribution models the probability of multiple consequent events occurring in a fixed interval of time, given a mean number of occurrences $\lambda$. The PDF is given in (34). Note that this is a discrete distribution and therefore the variable $k$ is used in place of $x$.

$$f_{\mathcal{P}}(k, \lambda) = \frac{\lambda^k e^{-\lambda}}{k!} \tag{34}$$

### A.2.5 *Triangular*

The triangular distribution is used when there is a knowledge of the minimum and maximum probability points.

$$f_{\mathcal{T}}(x,l,u,m) = \begin{cases} 0 & x \leq l \\ \frac{2(x-l)}{(u-l)(m-l)} & l < x \leq m \\ \frac{2(u-x)}{(u-l)(u-m)} & m < x \leq u \\ 0 & x > u \end{cases} \tag{35}$$

The PDF reported in (35) is indeed characterized by a triangular shape, which gives zero probability outside of the boundaries $l$ and $u$, and maximum at the triangle peak $m$.

### A.2.6 *Uniform Radius on Circle*

For a circular surface of radius $r$, to compute the probability of sampling a radius lower than a certain value $x$, one may think to increase $x$ from 0 till $\pi x^2$ reaches the total area $A = \pi r^2$. The CDF is then simply obtained by dividing this increasing area by $A$, as shown in (36), and the PDF is then obtained by deriving the CDF, as shown in (37).

$$F_{\mathcal{U}_{circ}}(x) = \begin{cases} \frac{\pi x^2}{A} & x < r_{max} \\ 1 & x \geq r_{max} \end{cases} \tag{36}$$

$$f_{\mathcal{U}_{circ}}(x) = \begin{cases} \frac{2\pi x}{A} & x < r_{max} \\ 0 & x \geq r_{max} \end{cases} \tag{37}$$

### A.2.7 *Uniform Radius on Polygon*

Consider the triangle in *Figure 12*, where $r_{in}$ radius of the inscribed circle and $r_{out}$ radius of the circumscribed circle. A $F_{\mathcal{U}_{circ}}$ distribution could still be used for a radius that increases up to the one corresponding to the red circle. After that, the area of the polygon that gets covered is lower and lower with respect to the theoretical circle, up to a radius corresponding to the green circle. Between $r_{in}$ and $r_{out}$ the area $S$ of each circular segment must be subtracted from the circular area of radius $x$. This area grows with $x$ and is given by (38).

$$\begin{aligned} S(x) &= \frac{1}{2}x^2\left(2\phi_{(x)} - \sin\left(2\phi_{(x)}\right)\right) \\ &= x^2\left(\phi_{(x)} - \sin\phi_{(x)}\cos\phi_{(x)}\right) \end{aligned} \tag{38}$$

Where the angle $\phi$ is given by (39)

$$\phi_{(x)} = \operatorname{acos}\left(\frac{r_{in}}{x}\right) \tag{39}$$

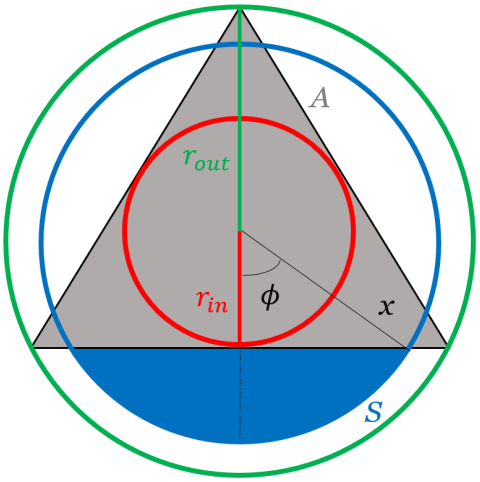


**Fig. 12 Derivation of the uniform distribution of radius on a triangle**

Considering a generic polygon with $n$ sides and area $A$, the CDF and PDF are then reported in (40) and in (41) respectively. Note that when $x = r_{out}$, $\phi = \frac{2\pi}{2n}$ and CDF and PDF goes respectively to 1 and 0 as expected.

$$F_{\mathcal{U}_{Poly}}(x) = \begin{cases} \frac{\pi x^2}{A} & x \leq r_{in} \\ \frac{\pi x^2}{A}\left[1 - \frac{n}{\pi}\left(\phi_{(x)} - \sin\phi_{(x)}\cos\phi_{(x)}\right)\right] & r_{in} < x \leq r_{out} \\ 1 & x > r_{out} \end{cases} \tag{40}$$

$$f_{\mathcal{U}_{Poly}}(x) = \begin{cases} \frac{2\pi x}{A} & x \leq r_{in} \\ \frac{2\pi x}{A}\left[1 - \frac{n}{\pi}\phi_{(x)}\right] & r_{in} < x \leq r_{out} \\ 0 & x > r_{out} \end{cases} \tag{41}$$

### A.3 Sampling

To generate samples from known distribution functions, a common method used is inverse transform sampling [19]. Given a uniform RV $U$ between 0 and 1, equation (42) can be used to obtain a RV $X$ that follows the distribution given by $F_X$.

$$X = F_X^{-1}(U) \tag{42}$$

This method has the drawback of relying on the existence of the inverse for the CDF, although due to its simplicity will be used in the MC campaign for sampling the RV used at each simulation.

## B Simulation

The models used for the MC campaign will be outlined in the following paragraphs.

### B.1 Dynamics

The dust impacts are assumed to be elastic and to not change the mass of the S/C nor its distribution, so the Mass, Center of Gravity and Inertia (MCI) properties remain constant throughout the simulation. Given the modelled relative encounter velocity, trajectories are expected to have a short duration, from 20 min up to 2 h, which also allows to simplify them as straight lines of constant speed. Therefore, the translational dynamics will be a rectilinear motion with uniform velocity, as given by (43). The attitude is propagated by integrating the rigid body and the passive RW dynamics in the same system, according to (44), where $\boldsymbol{T}_{ext}$ is the sum of all the external torques.

$$\begin{bmatrix} \ddot{s} \\ \dot{s} \end{bmatrix} = \begin{bmatrix} 0 \\ v \end{bmatrix} \tag{43}$$

$$\begin{bmatrix} & I & & \begin{Bmatrix} 0 \\ 0 \\ I_{RW} \end{Bmatrix} \\ \{0 & 0 & I_{RW}\} & I_{RW} \end{bmatrix} \begin{bmatrix} \dot{\boldsymbol{\omega}} \\ \dot{\omega}_{RW} \end{bmatrix} = \begin{bmatrix} \boldsymbol{T}_{ext} - \boldsymbol{\omega} \times \left( I\,\boldsymbol{\omega} + I_{RW} \begin{Bmatrix} 0 \\ 0 \\ \omega_{RW} \end{Bmatrix} \right) \\ 0 \end{bmatrix} \tag{44}$$

External disturbances can be restricted to just the ones caused by the dust particle impact on the probe surface. In fact, all the other disturbances such as Solar Radiation Pressure (SRP) or gravity perturbations caused by the comet or other celestial bodies, are negligible with respect to the discrete cumulative impacts contribution in the timescale considered.

## B.2 Impact Model

The impact model computes the angular momentum generated by the total number of particles impacting the s/c surface at each time step, obtained applying (45).

$$n = v\, A_{oct}\, t_s\, N_{num}(s, ca) \tag{45}$$

Where $s$ is the distance from CA at the current time step, $ca$ is fixed at each MC shot, $N_{num}$ is the numeric density extracted from the Look-Up Tables (LUT) at the corresponding $s$ and $ca$ breakpoints, $v$ is the impact velocity, $t_s$ is the simulation sampling time. Note that at each shot $ca$ and $v$ are sampled using inverse transform (see *subsection A.3*) from their modelled distributions and the numeric density LUT is re-scaled according to (9).

After $n$ is computed, its decimal part is retained and compared to a random uniform number $X_1 \sim \mathcal{U}_{[0,1]}$. The resulting boolean (0 or 1) is then added to the integer part such to maintain the correct probability of rounding, as shown in (46).

$$n_{int} = \lfloor n \rfloor + [(n - \lfloor n \rfloor) > X_1] \tag{46}$$

At this point an impact vector $\boldsymbol{r}_i$ and an impact mass $m_i$ are sampled iterating (47) and (48) at each $i = 1, \ldots, n_{int}$. The impact vector is scattered uniformly across the octagonal surface and the mass is sampled through inverse transform (see *subsection A.3*). A maximum number of 10 impacts per time step is considered for computational feasibility.

$$\boldsymbol{r}_i = p_{(r_{out},\psi)} \sqrt{Y_1} \begin{Bmatrix} \cos(\psi) \\ \sin(\psi) \\ 0 \end{Bmatrix} \qquad \text{where} \qquad \psi = 2\pi\, Y_2 \tag{47}$$

$$m_i = F_M^{-1}(Y_3) \tag{48}$$

Where $p_{(r_{out},\psi)}$ gives the perimetral radius of an octagon corresponding to angle $\theta$, $F_M(m)$ is the CDF of the impact mass, and $Y_j \sim \mathcal{U}_{[0,1]}$ for $j = 1, 2, 3$.

Finally, the angular momentum is computed and summed up using (49), where $\boldsymbol{r}_{\bullet}$ is the COG distance with respect to the center of the shield.

$$\boldsymbol{h}_{imp} = \sum_{i=1}^{n_{int}} m_i\, v\ (\boldsymbol{r}_i - \boldsymbol{r}_{\bullet}) \tag{49}$$

The momentum then enters the dynamics as an instantaneous torque, dividing it by the sample time as shown in (50).

$$\boldsymbol{T}_{ext} = \frac{\boldsymbol{h}_{imp}}{t_s} \tag{50}$$

# References


[1] T Ott, A Benoit, P Van den Braembussche, and W Fichter. Esa pointing error engineering handbook. In *8th International ESA Conference on Guidance, Navigation & Control Systems*, page 17, 2011.

[2] Massimo Casasco, Gonzalo Saavedra Criado, Sven Weikert, Jochen Eggert, Marc Hirth, Thomas Ott, and Haifeng Su. Pointing error budgeting for high pointing accuracy mission using the pointing error engineering tool. In *AIAA Guidance, Navigation, and Control (GNC) Conference*. American Institute of Aeronautics and Astronautics, aug 2013. DOI: 10.2514/6.2013-5251.

[3] T Ott, M Hirth, M Casasco, S Gedon, and A Ponche. Pointingsat–high precision pointing error analysis with esa peet v1. 0. In *10th International ESA Conference on Guidance, Navigation & Control Systems, Salzburg, Austria*, 2017.

[4] J. Doyle. Robust and optimal control. In *Proceedings of 35th IEEE Conference on Decision and Control*. IEEE, 1996. DOI: 10.1109/cdc.1996.572756.

[5] Sovanna Thai, Clément Roos, and Jean-Marc Biannic. Probabilistic mu-analysis for stability and h-inf performance verification. In *2019 American Control Conference (ACC)*, pages 3099–3104. IEEE, 2019. DOI: 10.23919/ACC.2019.8814315.

[6] Samir Bennani, Mathieu Claeys, Luca Massotti, Finn Ankersen, and Pierluigi Silvestrin. Preliminary aocs design for pointing budget assessment of the biomass candidate earth explorer core mission. *IFAC Proceedings Volumes*, 43(15):309–314, 2010. DOI: 10.3182/20100906-5-JP-2022.00053.

[7] Diego Navarro-Tapia, A Marcos, and Joost Veenman. Enhanced aocs verification techniques for euclid's high-pointing performance. *IFAC-PapersOnLine*, 55(25):91–96, 2022. DOI: 10.1016/j.ifacol.2022.09.329.

[8] Jean-Marc Biannic, Clement Roos, Samir Bennani, Fabrice Boquet, Valentin Preda, and Benedicte Girouart. Advanced probabilistic mu-analysis techniques for AOCS validation. *European Journal of Control*, 62:120–129, nov 2021. DOI: 10.1016/j.ejcon.2021.06.019.

[9] Luc B.M. Sagnieres and Inna Sharf. Stochastic modeling of hypervelocity impacts in attitude propagation of space debris. *Advances in Space Research*, 59(4):1128–1143, feb 2017. DOI: 10.1016/j.asr.2016.11.030.

[10] P. Machuca, N. Ozaki, J.P. Sánchez, and L. Felicetti. Dust impact and attitude analysis for JAXA's probe on the comet interceptor mission. *Advances in Space Research*, 70(5):1189–1208, sep 2022. DOI: 10.1016/j.asr.2022.05.070.

[11] NA Konan, O Kannengieser, and O Simonin. Stochastic modeling of the multiple rebound effects for particle–rough wall collisions. *International journal of multiphase flow*, 35(10):933–945, 2009.

[12] Raphael Marschall, Vladimir Zakharov, Cecilia Tubiana, Michael S. P. Kelley, and Vincenzo Della Corte. Dust hazard assessment using the engineering dust coma model of the comet interceptor mission. jul 2021. DOI: 10.5194/epsc2021-540.

[13] H. U. Keller, W. A. Delamere, W. F. Huebner, H. J. Reitsema, H. U. Schmidt, F. L. Whipple, K. Wilhelm, W. Curdt, R. Kramm, N. Thomas, C. Arpigny, C. Barbieri, R. M. Bonnet, S. Cazes, M. Coradini, C. B. Cosmovici, D. W. Hughes, C. Jamar, D. Malaise, K. Schmidt, W. K. H. Schmidt, and P. Seige. Comet p/halley's nucleus and its activity. In *Exploration of Halley's Comet*, pages 807–823. Springer Berlin Heidelberg, 1988. DOI: 10.1007/978-3-642-82971-0138.

[14] K Richter, Werner Curdt, and HU Keller. Velocity of individual large dust particles ejected from comet p/halley. *Astronomy and Astrophysics (ISSN 0004-6361), vol. 250, no. 2, Oct. 1991, p. 548-555. Research supported by BMFT.*, 250:548–555, 1991.

[15] Cuncurrent Design Facility. *COMET INTERCEPTOR Assessment of Mission to Intercept a Long Period Comet or Interplanetary Object*. ESA, 2019.

[16] Raphael Marschall, Vladimir Zakharov, Cecilia Tubiana, Michael S. P. Kelley, Carlos Corral van Damme, Colin Snodgrass, Geraint H. Jones, Stavro L. Ivanovski, Frank Postberg, Vincenzo Della Corte, Jean-Baptiste Vincent, Olga Muñoz, Fiorangela La Forgia, and Anny-Chantal Levasseur-Regourd and. Determining the dust environment of an unknown comet for a spacecraft flyby: The case of ESA's comet interceptor mission. *Astronomy And Astrophysics*, 666:A151, oct 2022. DOI: 10.1051/0004-6361/202243648.

[17] Nico Haslebacher, Selina-Barbara Gerig, Nicolas Thomas, Raphael Marschall, Vladimir Zakharov, and Cecilia Tubiana. A numerical model of dust particle impacts during a cometary encounter with application to ESA's comet interceptor mission. *Acta Astronautica*, 195:243–250, jun 2022. DOI: 10.1016/j.actaastro.2022.02.023.

[18] Thomas Maschberger and Pavel Kroupa. Estimators for the exponent and upper limit, and goodness-of-fit tests for (truncated) power-law distributions. *Monthly Notices of the Royal Astronomical Society*, 395(2):931–942, may 2009. DOI: 10.1111/j.1365-2966.2009.14577.x.

[19] Luc Devroye. Chapter 4 nonuniform random variate generation. In *Simulation*, pages 83–121. Elsevier, 2006. DOI: 10.1016/s0927-0507(06)13004-2.